



Enhanced electrochemical performance of $\text{Li}_{1.2}\text{Ni}_{0.2}\text{Mn}_{0.6-x}\text{Al}_x\text{O}_2$ cathodes in an in situ Li_2CO_3 coating by a one-step method

Yong-Lin Huo¹ · Yi-Jing Gu¹ · Zi-Liang Chen¹ · Xiao-Yu Ma¹ · Fu-Zhong Wu¹ · Xin-Yi Dai¹

Received: 3 August 2022 / Revised: 15 September 2022 / Accepted: 18 October 2022 / Published online: 24 October 2022
© The Author(s), under exclusive licence to Springer-Verlag GmbH Germany, part of Springer Nature 2022

Abstract

Cathodes must accommodate the excellent performance of the applied anodes in lithium batteries. Li-rich Mn-based cathode materials with a specific capacity beyond $250 \text{ mAh}\cdot\text{g}^{-1}$ are considered some of the most promising cathode materials, although they suffer from some unsolved problems. In this paper, a series of $\text{Li}_{1.2}\text{Ni}_{0.2}\text{Mn}_{0.6-x}\text{Al}_x\text{O}_2$ cathodes with an in situ-synthesized Li_2CO_3 coating layer by a one-step method is utilized to enhance their electrochemical performance by inhibiting the transition from a layered structure to a spinel structure and reducing the generation of Mn^{3+} . The $\text{Li}_{1.2}\text{Ni}_{0.2}\text{Mn}_{0.56}\text{Al}_{0.04}\text{O}_2@ \text{Li}_2\text{CO}_3$ coating sample exhibits an excellent capacity retention rate of 89.5% and a small voltage decay of 1.11 mV per cycle after 200 cycles at 1 C. Lithium-ion full cells composed of $\text{Li}_{1.2}\text{Ni}_{0.2}\text{Mn}_{0.56}\text{Al}_{0.04}\text{O}_2@ \text{Li}_2\text{CO}_3$ and graphite show an energy density of $443.7 \text{ Wh}\cdot\text{kg}^{-1}$ at 0.1 C, and the capacity retention rate is 95.6% after 200 cycles at 1 C. These results offer prospects for satisfying the high energy density requirements of electric equipment.

Keywords Lithium-ion battery · Cobalt-free · Li-rich Mn-based cathode materials · Al^{3+} doping

Introduction

All electrical equipment generated by lithium-ion batteries (LIBs) require higher electrical performance to satisfy the increasing demand [1–4], which requires the applied batteries to offer better cooperation between cathodes and anodes. Although great progress has been made in anode modification [5–8], cathode materials with higher energy densities are still needed to meet this goal. Thus, new cathodes must be explored. Li-rich Mn-based cathode materials are composed of LiMO_2 (where M represents Co, Ni, Mn, etc.) and Li_2MnO_3 , whose specific capacity can exceed $250 \text{ mAh}\cdot\text{g}^{-1}$ [9–11] beyond LiCoO_2 [12] and LiFePO_4 [13, 14]. It can be considered one of the most promising materials because Li_2MnO_3 can activate anion redox to generate another part of electrical energy above 4.5 V. If its initial Coulomb efficiency (ICE), voltage and capacity attenuation, and poor rate performance can further increase as the next-generation cathodes based on recent studies, Li-rich Mn-based cathode materials will replace the primary cathodes [15–18].

Many methods have been proposed to solve the aforementioned disadvantages of Li-rich Mn-based cathode materials, such as surface modification and ion doping. Surface modification, such as coating with carbon [10], metal oxides [19], fluorides [20], and phosphates [21], can inhibit the transformation of the surface structure from a layered structure to a spinel structure and mitigate the side reactions. Many experiments show that coating can improve the ICE and cycle stability [10, 19–22], but an additional coating process will increase the cost, which is unfavorable for industrialization. Ion doping is a simple modification method that does not increase the extra process and cost during the synthesis process. At present, researchers have utilized many constant-value elements to modify crystal lattices, such as Na [23], Mg [24], Al [25], Fe [26], and F [27], to obtain higher ICE performance, rate performance, and cycle stability.

Al is abundant in the Earth's crust and costs less than most metal elements. Al doping can enhance the cycle performance by stabilizing the crystal structure and inhibiting the reduction of transition metal (TM) cation [18, 28, 29]. Some researchers have reported that Al^{3+} doped at the Li site and TM site has achieved good rate performance and cycle stability [25, 30, 31]. For example, Nayak et al. [30] reported Al-doped Li-rich Mn-based cathode materials ($\text{Li}_{1.2}\text{Ni}_{0.16}\text{Mn}_{0.56}\text{Co}_{0.08}\text{O}_2$). They found that doping the Al

✉ Yi-Jing Gu
yijing-gu@163.com

¹ College of Materials and Metallurgy, Guizhou University, South Hua-Xi Street, Guiyang 550025, China

element decreased the specific capacity and significantly increased the capacity retention rate. Chen et al. [25] synthesized an Al-doped electrode material with a layered micro/nanostructure by using a porous polypropylene film as a hard template; they found that the $\text{Li}_{1.2}\text{Ni}_{0.18}\text{Mn}_{0.58}\text{Al}_{0.04}\text{O}_2$ sample provided the highest specific capacity, reduced the charge transfer resistance, and improved the rate performance, structural stability, and lithium-ion diffusion coefficient. Although there have been reports on Al-doped Li-rich Mn-based cathode materials, the relationship between voltage attenuation and the valence state of TM cations has not been studied, and the properties of this material at high temperature and lithium-ion full cells have not been provided, which are necessary for any material before applications [32]. Therefore, the effect of Al doping must be explored.

In addition, the coating process can increase the cost for enhancing the performance of LIBs, so it is meaningful to form a coating on the material surface without additional processes. In this work, we designed a modified Pechini method to synthesize a series of $\text{Li}_{1.2}\text{Ni}_{0.2}\text{Mn}_{0.6-x}\text{Al}_x\text{O}_2$ ($x=0, 0.02, 0.04, 0.06$) cathode materials with an Li_2CO_3 coating using a one-step synthesis method, and the corresponding schematic diagram is shown in Fig. 1. In these materials, a small amount of Mn was replaced by Al. Compared with the undoped samples, the doped samples have better voltage stability, capacity stability, temperature stability, and rate performance. In addition, we have researched how Al doping affects the structural transitions and TM cation valence reductions and explored the scientific truth.

Experimental section

Material synthesis

A series of materials was synthesized using a modified Pechini method. Stoichiometric amounts of $\text{Mn}(\text{CH}_3\text{COO})_2 \cdot 4\text{H}_2\text{O}$, $\text{Ni}(\text{CH}_3\text{COO})_2 \cdot 4\text{H}_2\text{O}$, and 5% excess $\text{LiCH}_2\text{COO} \cdot \text{H}_2\text{O}$ were mixed and dissolved in deionized water and subsequently dissolved in a mixed solution of citric acid (AC) and ethylene glycol (EG) (molar ratio = 1:4). The mixed solution was evaporated and dried to obtain a polymeric precursor. The undoped sample $\text{Li}_{1.2}\text{Ni}_{0.2}\text{Mn}_{0.6}\text{O}_2$ was obtained by 5 h of pre-sintering at 500°C and 12 h of sintering at 950°C in air, and it was named LRMA0. The synthesis process had the extra $\text{LiCH}_2\text{COO} \cdot \text{H}_2\text{O}$ and organic agents that could decompose to generate Li_2O and CO_2 to form an in situ Li_2CO_3 coating at high temperature. For the doped samples, the same stoichiometric aluminum acetate was used to replace the manganese acetate using the aforementioned synthesis steps. According to different doping amounts, $\text{Li}_{1.2}\text{Ni}_{0.2}\text{Mn}_{0.58}\text{Al}_{0.02}\text{O}_2$, $\text{Li}_{1.2}\text{Ni}_{0.2}\text{Mn}_{0.56}\text{Al}_{0.04}\text{O}_2$, and $\text{Li}_{1.2}\text{Ni}_{0.2}\text{Mn}_{0.54}\text{Al}_{0.06}\text{O}_2$ were synthesized and named LRMA2, LRMA4, and LRMA6, respectively.

Material characterizations

X-ray diffraction (XRD) was utilized to obtain the crystallographic structure and phase state of the materials with

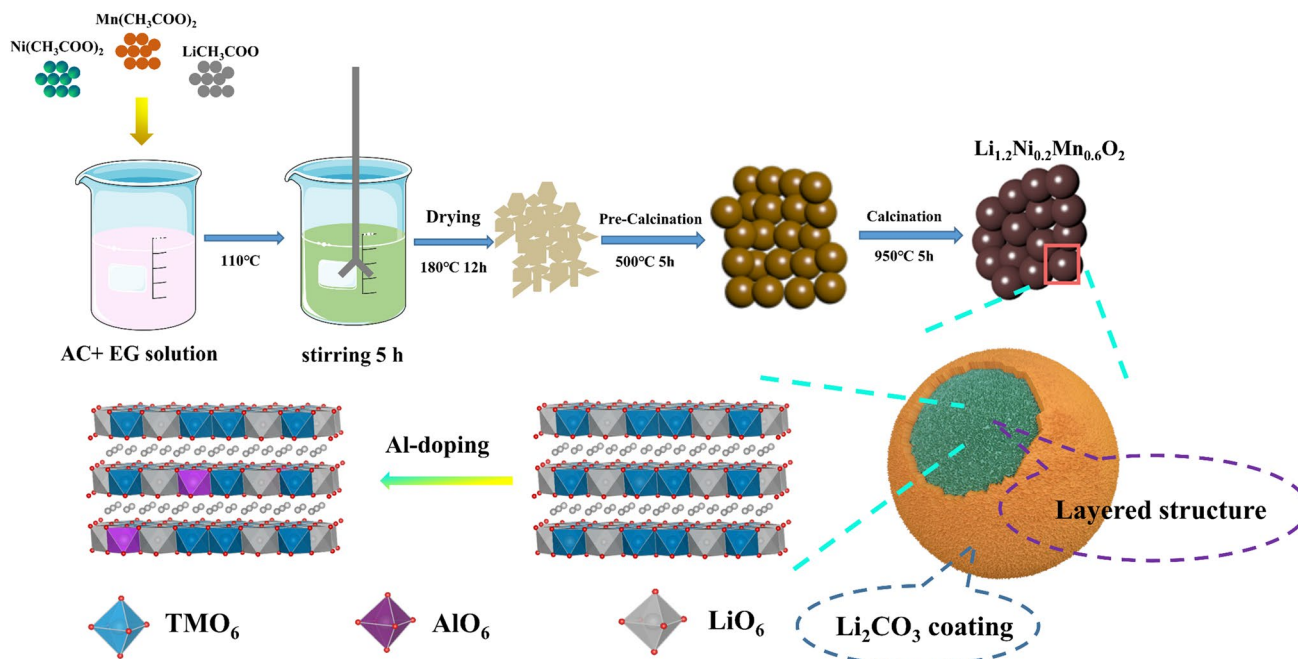


Fig. 1 The process of synthesizing the $\text{Li}_{1.2}\text{Ni}_{0.2}\text{Mn}_{0.6}\text{O}_2$ sample

Cu-K α radiation in a scanning range of 10–80° at a scanning rate of 5°/min. The general structural analysis software (GSAS) was used for the Rietveld refinement. The microstructure of the materials was characterized using scanning electron microscopy (SEM). The crystallinity and microstructure of the samples were characterized using transmission electron microscopy (TEM) and high-resolution transmission electron microscopy (HR-TEM). Raman spectroscopic studies of pristine and cycled electrodes were performed by a Raman spectrometer equipped with a 532-nm laser. X-ray photoelectron spectroscopy (XPS) was used to analyze the distribution of elemental species and valence states on the surfaces of the samples, and the spectra of all elements were calibrated with the C1s peak at 284.8 eV.

Electrochemical measurements

The electrochemical properties of the synthesized materials were evaluated with CR-2032 coin-type half-cells. The active material, acetylene black, and polyvinylidene fluoride (PVDF) were uniformly mixed in N-methyl-2-pyrrolidone (NMP) at a weight ratio of 8:1:1 to prepare the electrode slurry. Then, the mixed slurry was uniformly smeared onto aluminum foil and dried at 110 °C overnight in a vacuum oven. The electrode materials were punched into small circles with a diameter of 10 mm. The CR-2032 coin-type half-cells were assembled in an argon glove box ($\text{H}_2\text{O} \leq 0.01$ ppm, $\text{O}_2 \leq 0.01$ ppm). Lithium metal was used as the counter electrode, Celgard 2400 was used as the diaphragm, and 1-M LiPF₆ dissolved in a mixture of ethylene carbonate (EC) and methyl carbonate (DMC) (EC: DMC = 1:1) was used as the electrolyte. The galvanostatic charge–discharge test of the coin-type half-cells was performed on the Land CT-2001A test system at different rates (1 C = 200 mAh·g⁻¹), and the voltage range was 2–4.8 V vs. Li/Li⁺. An electrochemical workstation (Chenhua) was used to measure the AC impedance of the coin-type half-cells at 0.1 Hz–100 kHz with an AC amplitude of 5 mV. Cyclic voltammetry (CV) was performed on a multi-channel electrochemical workstation. Lithium-ion full cells were tested in 2032-type coin cells. The negative electrodes were made up of graphite (80% wt%), PVDF (10 wt%), and acetylene black (10 wt%). In these full cells, the mass ratio of the negative electrode to the positive electrode (N/P) was approximately 1.10.

Results and discussions

Figure 2a shows the XRD patterns of all samples (LRMA0, LRMA2, LRMA4, and LRMA6). The main diffraction peaks correspond to the typical α -NaFeO₂ layered structure with the R-3 m space group [33, 34]. A few diffraction peaks

in the range of 20–23° can be considered the characteristic peak of Li₂MnO₃ with the C 2/m space group [35], as described in Fig. 2b. These weak diffraction peaks were caused by the orderly arrangement of Li and Mn in the TM layer. In addition, the peaks of (006)/(102) and (018)/(110) in the XRD patterns were noticeably split, which reveals that each material had an excellent layered structure [36]. Compared with the XRD patterns of the LRMA0 sample, no other diffraction peaks were found in the LRMA2, LRMA4, and LRMA6 samples, which suggest that Al successfully substituted Mn without forming a distinct impurity phase. After a careful analysis of the XRD patterns, a slight variation was observed: the 003 and 104 peaks shifted toward a large angle with the increase in doping amount of Al, as described in Figs. 2c and d. The shift of the Al-doped samples occurred because larger Ni²⁺ ($r = 0.69$ Å) was oxidized to smaller Ni³⁺ ($r = 0.56$ Å) due to the charge compensation effect of Al³⁺ substituting Mn⁴⁺ [30]. The corresponding variations in lattice parameters of all samples were calculated by Rietveld refinement. The fitted images and data are listed in Figs. 2e–h and Table 1. Lattice parameters “a” and “c” of the material gradually decreased with increasing doping amount, which is consistent with the variation in Figs. 2c and d. The c/a ratios of all samples were greater than 4.9, which further indicates an excellent layered structure [37]. The ratio of the diffraction peak intensity $I_{(003)}/I_{(104)}$ is usually associated with the degree of cation mixing in cathode materials. When the ratio is greater than 1.2, the material has a low degree of cation mixing and highly ordered layered structures [38]. Obviously, the ratios of all samples were greater than 1.2, which indicates that the degree of cation mixing was negligible. These results indicate that a small amount of Al doping will not change the layered crystal structure.

The SEM images of all samples are shown in Figs. 3a–d. The LRMA0 sample had the smallest particle size and the clearest edges. The LRMA0 sample had a more uniform particle size distribution (200–500 nm) than the others. The particle size of the doped samples increased with increasing amounts of doped Al, and there was a vaguely light-gossamer coating on the particles in Figs. 3b and c.

Figures 4a and b show the structural information of the LRMA0 sample measured by TEM and HR-TEM images. In Fig. 4a, we did not observe an obvious coating, but the HR-TEM image in Fig. 4b clearly shows a coating of approximately 1.5 nm on the surface. The reason may be that the coating layer was too thin to be found in TEM images. Figs. 4c and d show the structural information of the LRMA4 sample measured by TEM and HR-TEM images. Fig. 4c shows a coating with a thickness of approximately 2.5 nm outside the grain, which can be more clearly observed in the HR-TEM images of Fig. 4d. The coating may be the pursued Li₂CO₃ because the generated chemical

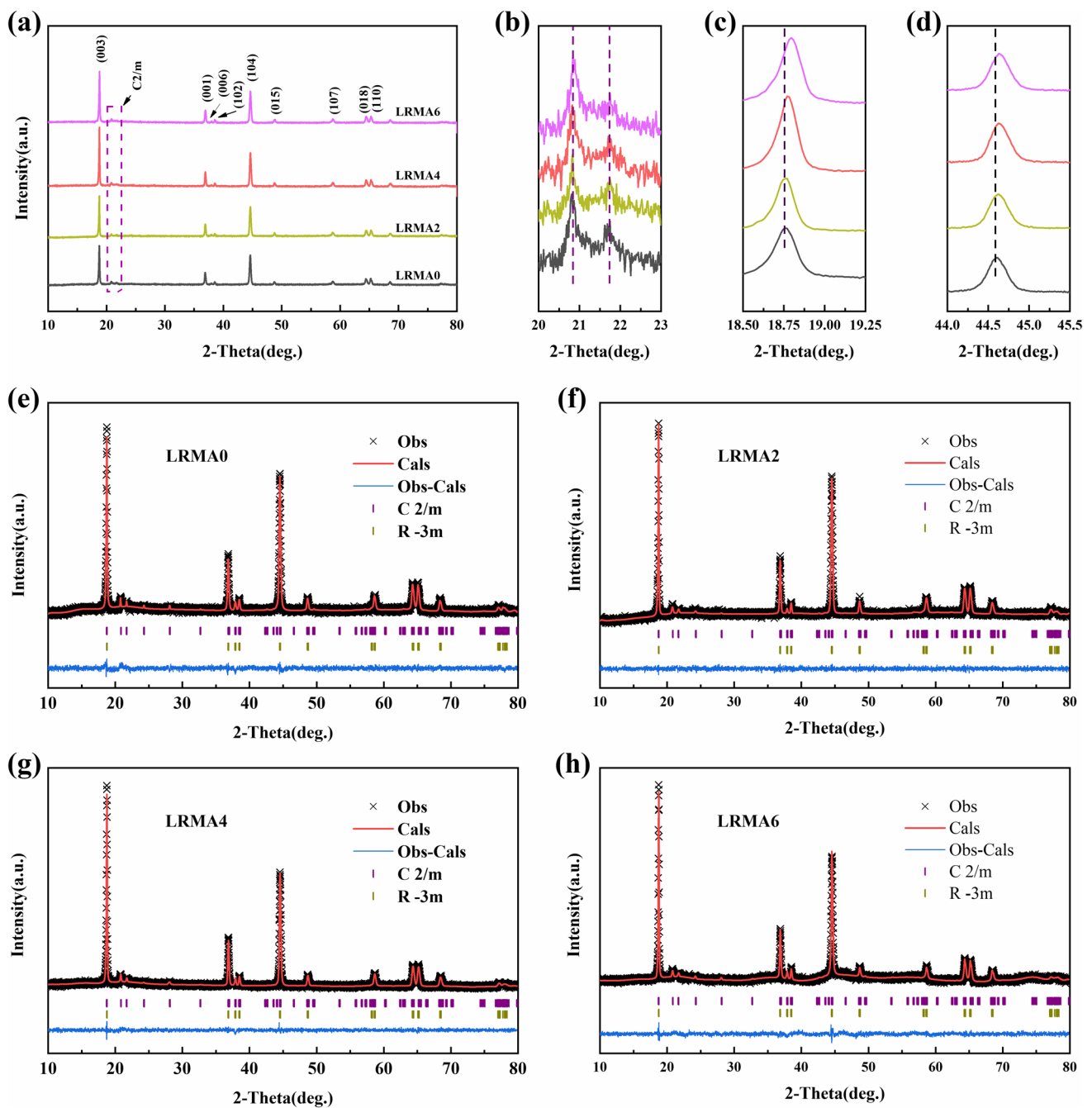
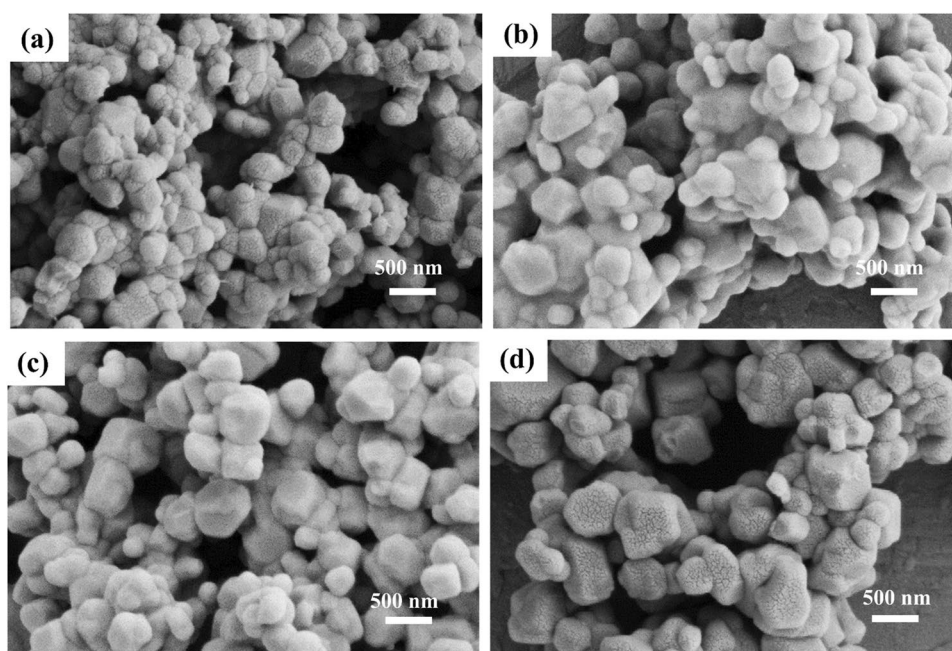


Fig. 2 A XRD patterns of LRMA0, LRMA2, LRMA4, and LRMA6 samples, **b–d** the corresponding enlarged XRD patterns, Rietveld refinement results of **e** LRMA0, **f** LRMA2, **g** LRMA4, and **h** LRMA4 samples

Table 1 Rietveld refinement data for as-prepared materials

Sample	a = b (Å)	c (Å)	Volume (Å ³)	I ₀₀₃ /I ₁₀₄	c/a	R _p	R _{wp}
LRMA0	2.8683	14.2926	101.838	1.24	4.983	2.29	2.88
LRMA2	2.8671	14.2909	101.739	1.28	4.984	2.18	2.74
LRMA4	2.8668	14.2886	101.702	1.59	4.984	2.16	2.72
LRMA6	2.8664	14.2860	101.657	1.47	4.984	2.13	2.67

Fig. 3 SEM images of **a** LRMA0, **b** LRMA2, **c** LRMA4, and **d** LRMA6



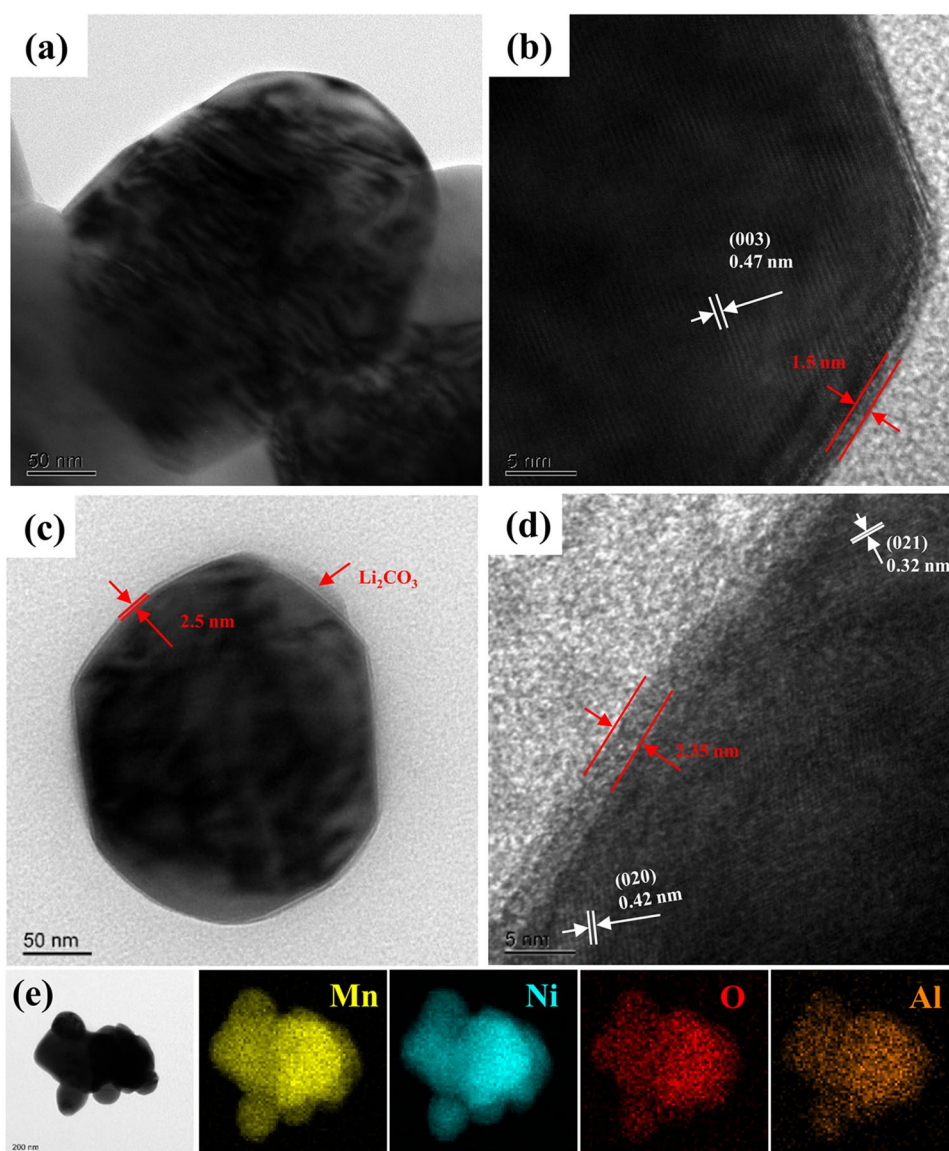
reaction formula is $\text{Li}_2\text{O} + \text{CO}_2 = \text{Li}_2\text{CO}_3$, where Li_2O and CO_2 could come from the decomposition of lithium acetate and other organic matter at high temperature. The Li_2CO_3 coating can hinder the direct contact between electrode and electrolyte and act as an artificial CEI film to reduce the loss of active material due to the spontaneous formation of the CEI film during the cycling process. In addition, due to the formation of a more stable CEI film on the surface, the surface side reaction in the cycling process is significantly inhibited, which effectively improves the electrochemical performance of the material [12]. Fig. 4b shows that the interplanar spacing was 0.47 nm, which corresponded to the (003) crystal planes. Fig. 4d shows that the interplanar spacings were 0.42 nm and 0.32 nm, which corresponded to the (020) and (021) crystal planes, respectively. These two crystal planes belong to the Li_2MnO_3 component, and the space group of this component is C 2/m. The characteristic peak of C 2/m is clearly visible in the XRD spectrum, but it was not treated in the spectrum because of its low component. To prove that the doped element was evenly distributed, EDS mapping of the LRMA4 sample is shown in Fig. 4e. Mn, Ni, O, and Al elements were present and evenly distributed in the material.

XPS was used to directly evaluate the surface chemical composition and valence change of the LRMA0 and LRMA4 samples, as shown in Fig. 5. The spectra of the LRMA0 and LRMA4 samples are displayed in Fig. 5a. Figures 5b–f show the XPS spectra of Al 2p, Ni 2p, Mn 2p, O 1s, and Li 1s. The Al 2p spectra of the LRMA0 and LRMA4 samples are shown in Fig. 5b. The LRMA0 sample did not have an Al 2p peak, which suggests that the sample did not contain Al. The LRMA4 sample had an Al 2p peak, which illustrates

that Al^{3+} was successfully doped into the lattice. In Fig. 5c, the binding energies of the Ni 2p_{3/2} and Ni 2p_{1/2} peaks were 854.8 eV and 872.5 eV [39], respectively. Two fitting peaks at 854.6 and 856 eV were obtained. The peak at 856 eV was indexed to Ni^{2+} , and the peak at 854.6 eV was indexed to Ni^{3+} [40, 41]. The fitting results illustrate that both LRMA0 and LRMA4 samples contained Ni^{2+} and Ni^{3+} , and LRMA4 had more Ni^{3+} . This result corresponds to the change in the XRD pattern. Fig. 5d displays the Mn 2p spectra of samples LRMA0 and LRMA4, and the two main peaks at binding energies of 654 eV and 642 eV correspond to the peaks of Mn 2p_{1/2} and Mn 2p_{3/2} in previous literature [42], where the Mn 2p_{3/2} peak can be divided into two peaks: the peak with a higher binding energy is Mn^{4+} , and the peak with a lower binding energy is Mn^{3+} . The fitting result suggests that Mn^{4+} had no significant change in the LRMA0 and LRMA4 samples. Fig. 5e depicts the O 1s XPS spectra of the LRMA0 and LRMA4 samples. The O 1s spectrum mainly included the M–O bond (where m represents a TM cation) at 229.2 eV [43, 44], and the peak at 531.2 eV can be ascribed to the C=O bond in carbonate species (Li_2CO_3); Yin et al. [45] reported a similar situation in which Li_2CO_3 coating appeared on the material surface. The result reveals an Li_2CO_3 coating on the surface of LRMA4 according to the design of the in situ coating synthesis. Fig. 5f shows the Li 1s XPS spectra of the LRMA0 and LRMA4 samples, where the Li_2CO_3 peak appeared at 55.3 eV for LRMA0 and LRMA4. This result is consistent with those reported in the literature [12]. Thus, the samples in this work had a thin Li_2CO_3 coating due to the one-step synthesis method.

Figs. 6a and b show the first charge–discharge curves and differential capacity vs. voltage (dQ/dV) profiles of all

Fig. 4 TEM images of LRMA0 **a** TEM, **b** HR-TEM. TEM images of LRMA4 **c** TEM, **d** HR-TEM, **e** the element mapping images of LRMA4



samples. The charge–discharge rate was 0.1 C, and the voltage range was 2–4.8 V. The charging curves of all samples were divided into two parts: the inclined region below 4.5 V and the plateau area above 4.5 V. The inclined region was attributed to the reversible extraction of Li⁺ from the Li layer in LiMO₂ (M = Ni, Mn) and the oxidation from Ni²⁺ and Ni³⁺ to Ni⁴⁺ corresponding to the oxidation peak before 4.5 V in the dQ/dV profiles. The plateau area is related to the activation process of the Li₂MnO₃ component to remove Li₂O, since the sharp oxidation peak was at 4.5 V in the dQ/dV profiles [18] [10]. The dQ/dV profiles of the subsequent reduction process exhibit three reduction peaks: the reduction peak at 4.5 V corresponds to the reduction of O⁻ to O²⁻; the reduction peak near 3.7 V is attributed to the reduction of Ni⁴⁺; and the peak at 3.3 V is attributed to the reduction of Mn⁴⁺ to Mn³⁺ [39]. With the increase in Al

doping amount, the first discharge specific capacity of the material decreased. The first discharge specific capacities were approximately 268.2 mAh·g⁻¹, 262.2 mAh·g⁻¹, 258.6 mAh·g⁻¹, and 253.6 mAh·g⁻¹ for the LRMA0, LRMA2, LRMA4, and LRMA6 samples, respectively. The specific capacity decreased because Al is inert compared to Ni and Mn, which reduced the active mass. When Co is substituted by Al, similar results will be produced [46]. The ICE is found to be 78.3%, 78.9%, 79.0%, and 78.7% for LRMA0, LRMA2, LRMA4, and LRMA6, respectively. The ICE did not greatly change with the Al doping.

To evaluate the influence of Al doping on the cyclic performance, the tests of all samples were measured at 1 C for 200 cycles after the cell was activated at 0.1 C for three cycles in a voltage range of 2–4.8 V (2–4.65 V for the 1st cycle) in Fig. 6c. The specific capacities of the LRMA0,

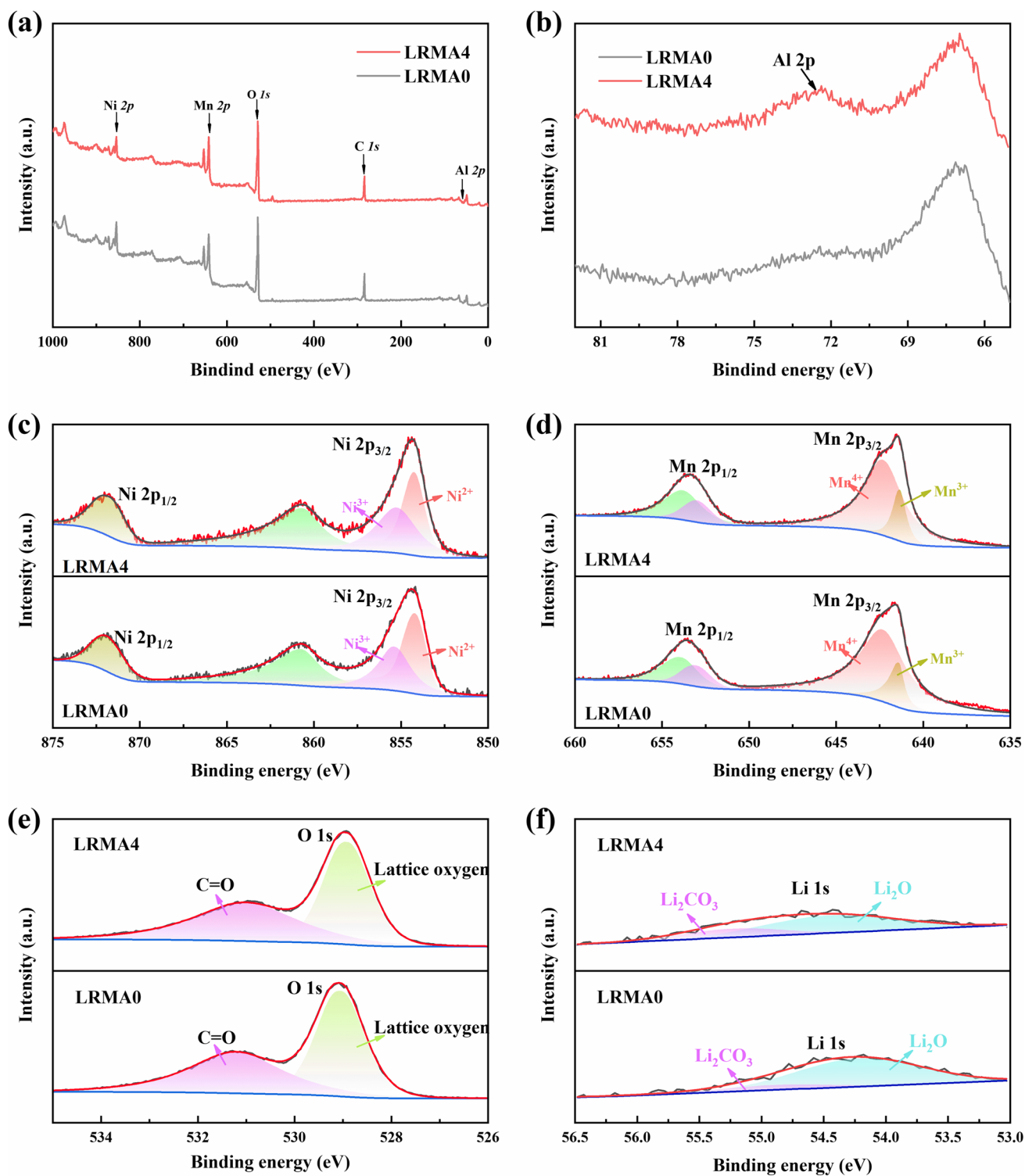


Fig. 5 XPS spectra of **a** survey scan, **b** Al2p, **c** Ni2p, **d** Mn2p, **e** O1s, and **f** Li1s for LRMA0 and LRMA4 samples

LRMA2, LRMA4, and LRMA6 samples were approximately 188.5 mAh·g⁻¹, 192.6 mAh·g⁻¹, 193.1 mAh·g⁻¹, and 190 mAh·g⁻¹ with capacity retentions of 63.2%, 76.2%, 89.5%, and 81.1% after 200 cycles, respectively. The relationship

between the discharge medium voltage (DMV) of the four cathode materials and the number of cycles is described in Fig. 6d. After 200 cycles, the DMV of LRMA0 dropped from 3.564 to 3.177 V with a DMV decay of 1.94 mV per

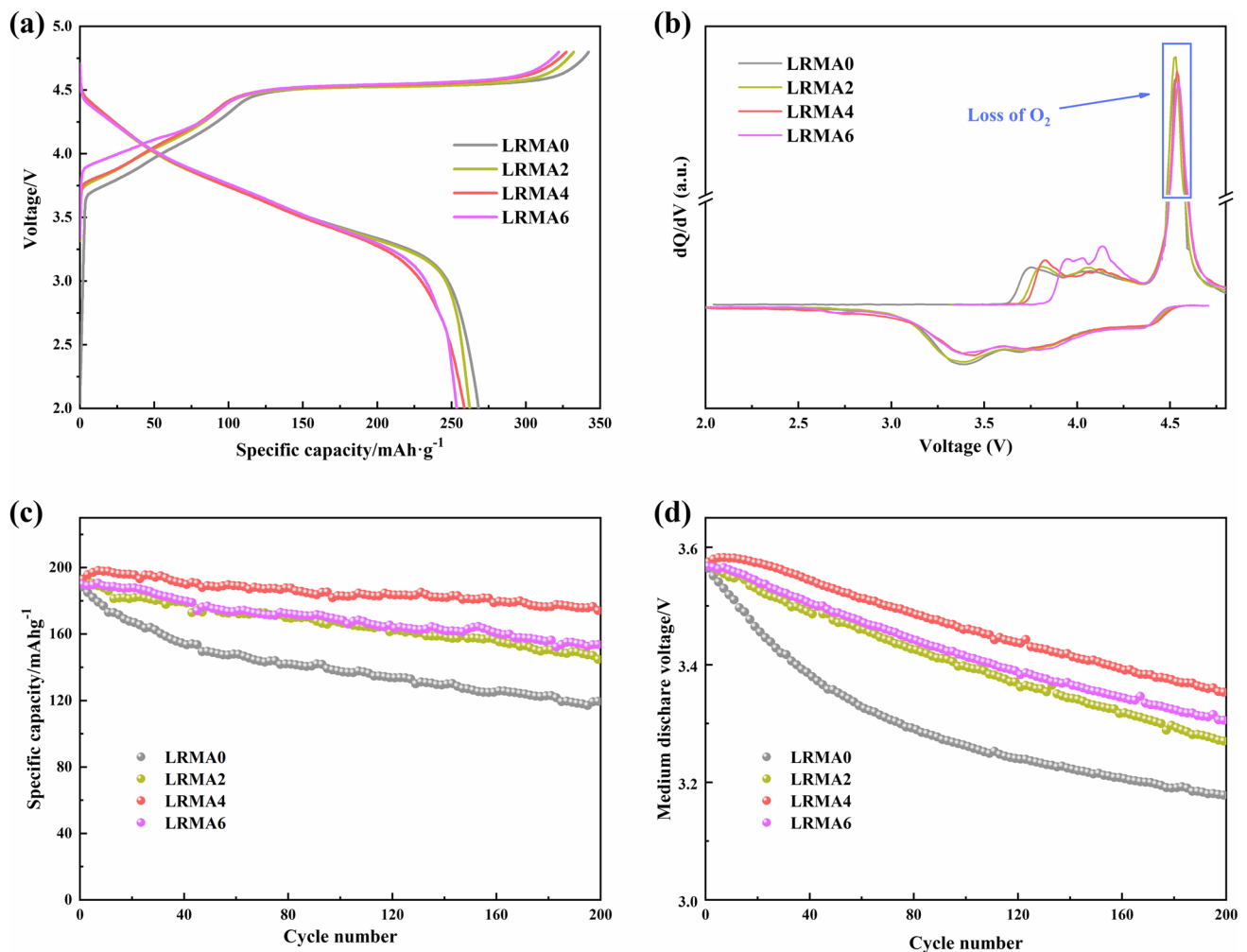


Fig. 6 **a** First charge–discharge curves. **b** The corresponding dQ/dV curves at the first cycle. **c** Cycling stability and **d** voltage fading of the LRMA0, LRMA2, LRMA4, and LRMA6 samples

cycle. The attenuation of the DMV for LRMA2, LRMA4, and LRMA6 decreased from 3.571 to 3.268 V, from 3.575 to 3.353 V, and from 3.567 to 3.304 V, for which the DMV decays were 1.52 mV, 1.11 mV, and 1.32 mV per cycle, respectively. Fig. 7 shows the charge–discharge curves at 1 C. The specific capacity of LRMA4 above 3 V was 128.7 mAh·g⁻¹, while the specific capacities of LRMA0, LRMA2, and LRMA6 were 74.4 mAh·g⁻¹, 103.3 mAh·g⁻¹, and 109.2 mAh·g⁻¹, respectively. The capacity and voltage stability of Al-doped samples significantly improved. A possible reason is that the strong Al–O bond reduced the oxygen release during the cycle process [46, 47], which inhibited the reduction of the average valence state of the TM cation. The result can be affirmed by the latest research that the continuous release of oxygen reduces the average valence state of TM cations during the cycle measurements, which directly causes the voltage decay [47, 48]. In the discussion of XRD, doping Al can increase the amount of Ni³⁺, which can reduce the

unit cell parameters. It is favorable to inhibit the free migration of TM cations to the Li layer and slow the problematic phase transition [30]. Furthermore, Li₂CO₃ can form a stable CEI film on the surface of the material, inhibit the side reaction on the surface, and reduce the polarization during circulation. This is beneficial to enhance the cycle stability [6]. Table 2 compares the electrochemical performances of Li-rich Mn-based cathode materials obtained in recent years [36, 46, 49–55]. Compared with other reported batteries, the batteries in this paper have quite excellent performance. In particular, compared with the Al-doped sample made by Fu et al., because the sample in this work had a Li₂CO₃ coating, our samples had better performance. In summary, doping Al can improve the cyclic stability and mitigate the DMV decay of pristine samples. According to the results, LRMA4 has the highest capacity retention rate and the lowest DMV decay.

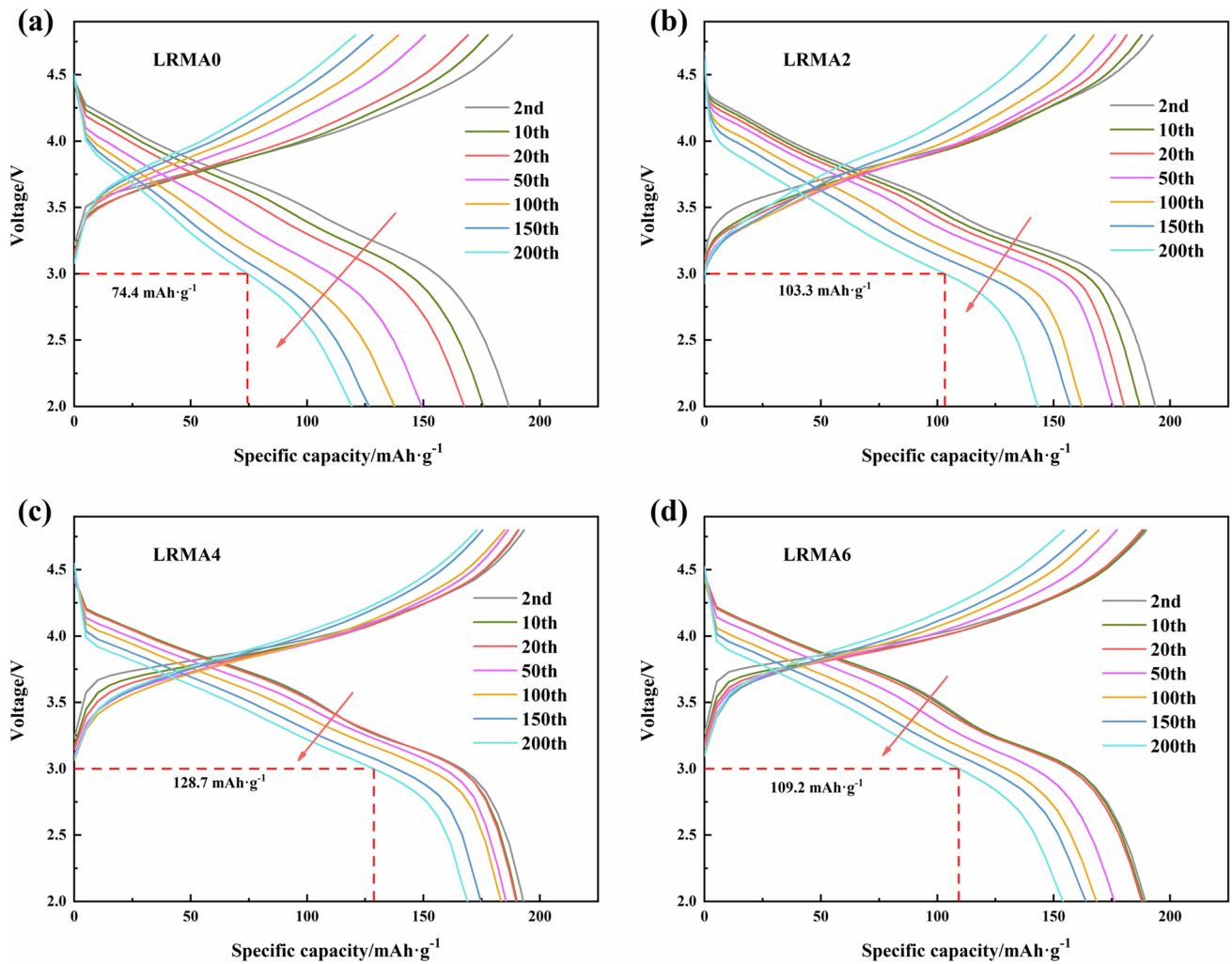


Fig. 7 Selected charge/discharge potential profiles of the **a** LRMA0, **b** LRMA2, **c** LRMA4, and **d** LRMA6 samples at 1 C

Table 2 Comparison of the electrochemical performance of Li-rich Mn-based cathode materials

Cathode materials	Modification	Measurement	Cycle	Cycle performance	Voltage decay per cycle	Ref
$\text{Li}_{1.15}\text{Na}_{0.05}\text{Mn}_{0.54}\text{Ni}_{0.13}\text{Co}_{0.13}\text{O}_{1.95}\text{F}_{0.05}$	Na, F co-doping	2.0–4.8 V, 1C	300	84.8%	1.99 mV	[36]
$\text{Li}_{1.2}\text{Ni}_{0.2}\text{Mn}_{0.6}\text{O}_2\text{Cd}_{0.03}\text{S}_{0.03}$	Gd, S co-doping	2.0–4.8 V, 1C	200	84.4%	2.5 mV	[37]
$\text{Li}_{1.20}\text{Mn}_{0.56}\text{Ni}_{0.16}\text{Co}_{0.08}\text{Fe}_{0.01}\text{P}_{0.0067}\text{O}_2$	Fe, PO_4^{3-} co-doping	2.0–4.8 V, 1C	130	88.4%	2.12 mV	[38]
$\text{Li}_{1.2}\text{Mn}_{0.53}\text{Ni}_{0.27}\text{O}_{1.97}\text{Cl}_{0.024}$	Cl doping	2.0–4.65 V, 1 C	300	75.7%	1.73 mV	[27]
$\text{LiNa}_{0.1}\text{Mn}_{0.56}\text{Ni}_{0.16}\text{Co}_{0.08}\text{O}_2$	Na doping	2.5–4.6 V, 0.5 C	100	93.5%	1.5 mV	[39]
$\text{Li}_{1.2}\text{Mn}_{0.533}\text{Ni}_{0.267}\text{Al}_x\text{Nd}_y\text{O}_2$	Al, Nd co-doping	2–4.65 V, 1 C	200	82%	1.84 mV	[40]
$(\text{Li}_{1.2}\text{Mn}_{0.525}\text{Ni}_{0.136}\text{Co}_{0.136}\text{Ce}_{0.015})_{0.985}\text{B}_{0.015}\text{O}_2$	Ce, B co-doping	2.2–4.8 V, 1 C	100	90.1%	2.26 mV	[41]
$\text{Li}_{1.171}\text{Cr}_{0.039}(\text{Ni}_{0.191}\text{Co}_{0.099}\text{Mn}_{0.539})\text{O}_2$	Cr doping	2.5–4.8 V, 0.1 C	100	86%	1.54 mV	[42]
$\text{Li}(\text{Li}_{0.2}\text{Ni}_{0.13}\text{Co}_{0.13}\text{Mn}_{0.52}\text{Al}_{0.02})\text{O}_2$	Al doping	2.0–4.8 V, 0.2 C	100	85.5%	4.9 mV	[33]
$\text{Li}_{1.2}\text{Ni}_{0.2}\text{Mn}_{0.56}\text{Al}_{0.04}\text{O}_2$	Al doping	2.0–4.8 V, 1 C	200	89.5%	1.11 mV	This work

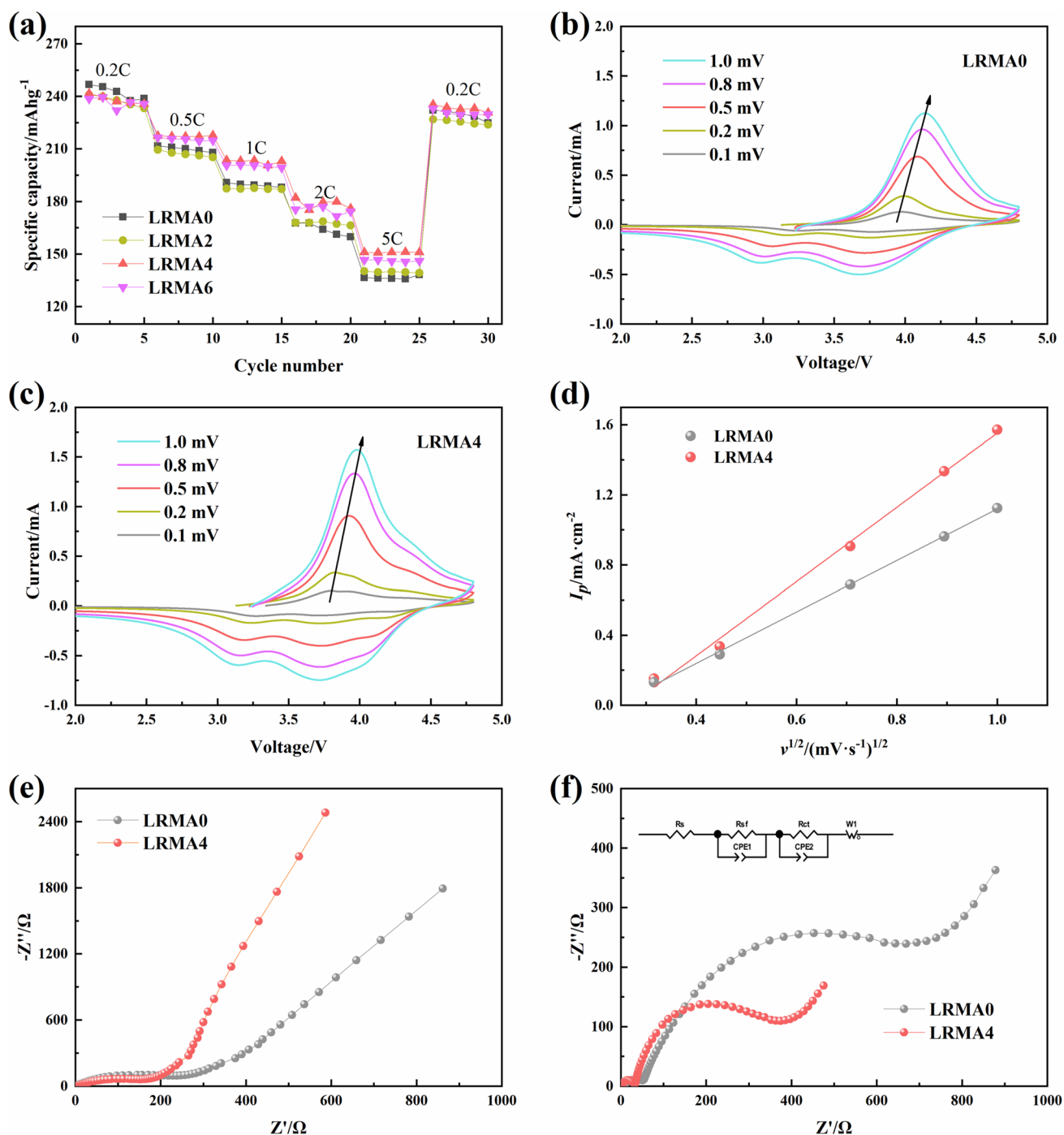


Fig. 8 a Rate capability of the LRMA0, LRMA2, LRMA4, and LRMA6 samples at different rates. CV profiles of **b** LRMA0 and **c** LRMA4 samples with various sweeping rates from 0.1 to 1 $\text{mV}\cdot\text{s}^{-1}$,

d $I_p - v^{1/2}$ relationships for both samples. Nyquist diagrams of the LRMA0 and LRMA4 samples **e** before cycling and **f** after 200 cycles at 1C

Figure 8a shows the rate capability of all samples. The rate performance was tested at current densities of 0.2 C, 0.5 C, 1 C, 2 C, 5 C, and 0.2 C. Obviously, the doped samples had slightly lower specific capacities than the undoped sample at low current densities, but with increasing current densities, the specific capacity of the doped samples gradually

exceeded that of the undoped sample. In particular, compared with $246.8 \text{ mAh}\cdot\text{g}^{-1}$, $211.6 \text{ mAh}\cdot\text{g}^{-1}$, $190.7 \text{ mAh}\cdot\text{g}^{-1}$, $167.6 \text{ mAh}\cdot\text{g}^{-1}$, and $136.4 \text{ mAh}\cdot\text{g}^{-1}$ for the LRMA0 sample, the LRMA4 sample showed capacities of $241.6 \text{ mAh}\cdot\text{g}^{-1}$, $217.5 \text{ mAh}\cdot\text{g}^{-1}$, $203.5 \text{ mAh}\cdot\text{g}^{-1}$, $182 \text{ mAh}\cdot\text{g}^{-1}$, and $151 \text{ mAh}\cdot\text{g}^{-1}$ at 0.2 C, 0.5 C, 1 C, 2 C, and 5 C, respectively.

After the high current density test, the capacity of all samples was well recovered to 0.2 C, and the specific capacity of the LRMA4 sample was recovered to 235.4 mAh·g⁻¹, which is higher than that of the LRMA0 sample (232.1 mAh·g⁻¹), which illustrates that the LRMA4 sample had better structural stability and capacity retention rate after the rapid Li⁺ insertion/extraction process. Al doping slightly improves the rate performance of the samples because the lithium-ion diffusion coefficient increases with increasing Al amount, as shown in Figs. 8b–d.

Fig. 8b–d show the CV experiments of LRMA0 and LRMA4 electrodes in the range of 0.1–1 mV to further investigate the influence of Al doping on the lithium-ion diffusion kinetics. The lithium-ion diffusion coefficient was calculated according to the following Randles – Sevcik equation [56]:

$$I_p = (2.69 \times 10^5) n^{3/2} C_{Li} A D_{Li}^{1/2} v^{1/2}$$

I_p is the peak current at specific scanning rates, n is the number of transferred electrons, C_{Li} is the molar concentration of Li⁺ in the cathode material, A is the electrode area, D_{Li} is the lithium-ion diffusion coefficient, and v is the scanning rate. According to Randles – Sevcik equation, we fit a straight line, which reflects the value of D_{Li} , as shown in Fig. 8d. The lithium-ion diffusion coefficients of the LRMA0 and LRMA4 electrodes were 1.07×10^{-12} cm²·s⁻¹ and 2.22×10^{-12} cm²·s⁻¹, respectively. The results show that the lithium-ion diffusion coefficient improved after the Al doping. The electrochemical behavior of doped Al was also investigated, and electrochemical impedance spectroscopy (EIS) tests of the LRMA0 and LRMA4 samples were performed. Fig. 8e shows the Nyquist plots of the LRMA0 and LRMA4 samples, which consisted of a semicircle and a line before cycling. The high-frequency region semicircle reflects the charge transfer impedance (R_{ct}), and the low-frequency region diagonal line represents Weber impedance. Fig. 8f displays the Nyquist plots for LRMA0 and LRMA4 samples, which consisted of two semicircles and a line after 200 cycles at 1 C. The high-frequency region semicircle corresponds to the surface film impedance (R_{sf}), the intermediate-frequency region semicircle corresponds to the charge transfer impedance (R_{ct}), and the low-frequency region diagonal line is associated with the diffusion of lithium ions in

the crystal lattice [23]. Table 3 shows the impedance fitting values of the LRMA0 and LRMA4 samples. The R_{ct} values of the LRMA0 and LRMA4 samples before cycling were 252.5 Ω and 130.2 Ω, respectively, which suggests that the LRMA4 sample had better electrochemical kinetics. After 200 cycles, the R_{sf} values of the LRMA0 and LRMA4 samples were 48.5 Ω and 27.4 Ω, and the R_{ct} values of the LRMA0 and LRMA4 samples were 627.5 Ω and 270.8 Ω, respectively. Although the impedance of the LRMA0 and LRMA4 samples increased after cycling, the difference was obvious. For comparison, the impedance increase of the LRMA4 sample was lower during cycling.

To further understand the fundamental reasons for the difference in electrochemical properties of materials, ex situ XRD analysis was conducted for the LRMA0 and LRMA4 samples after 200 cycles, as shown in Fig. 9a. If the diffraction peaks become broader and less intense, it is suggested that the crystal structure of the sample is distorted. For comparison, the XRD diffraction peaks of the LRMA4 sample had a smaller change, which indicates that the LRMA4 sample had less structural change. Furthermore, the ratio of I_{003}/I_{104} is usually used to indicate the degree of cation mixing [56]. In contrast, the ratio of LRMA0 was lower than 1.2, which implies its higher cation mixing degree. Fig. 9b shows the Raman spectra of LRMA0 and LRMA4 before cycling. The LRMA0 and LRMA4 samples showed two distinct Raman peaks near 482 and 600 cm⁻¹, which were indexed to the E_g bending and A_{1g} stretching of the layered hexagonal R-3 m symmetry. The weak peaks at 425 cm⁻¹ were attributed to the fingerprint vibration of Li₂MnO₃ with the C2/m space group. The Raman spectra of the LRMA0 and LRMA4 samples after 200 cycles are shown in Fig. 9c. Compared with the Raman spectrum before cycling, the peak at 425 cm⁻¹ disappeared, since the Li₂MnO₃ phase disappeared during cycling. Moreover, the LRMA0 and LRMA4 samples before cycling near 600 cm⁻¹ shifted to 622 cm⁻¹ and 604 cm⁻¹ in the spectra of the LRMA0 and LRMA4 samples after cycling measurements. This is the blueshift in Raman spectra after the cycling measurement of Li-rich manganese-based materials [57]. The slight blueshift in the Raman spectra of these Li-rich manganese-based materials is associated with the formation of the spinel phase during cycling. More blueshift corresponds to more spinel phase. In this connection, Al-doped Li-rich manganese-based materials can obviously inhibit the transition from the layer to the spinel phase; hence, they can improve the electrochemical performance because Al doping reduces the lattice parameters and inhibits the migration of TM ions [46, 58].

Fig. 9d–f show the XPS spectra of LRMA0 and LRMA4 after 200 cycles. In the XPS spectrum of Fig. 9d, F, N, and P elements were additionally detected compared with the spectrum of Fig. 5a before the cycle measurement. Elements F and P came from the electrolyte LiPF₆, and

Table 3 The fitted data from EIS spectra and the lithium-ion diffusion coefficient is calculated by the variable scanning speed CV

Sample	Before cycling	200th		D_{Li}^+ (cm ² ·s ⁻¹)
	R_{ct} (Ω)	R_{sf} (Ω)	R_{ct} (Ω)	
LRMA0	252.5	48.5	627.5	1.07×10^{-12}
LRMA4	130.2	27.4	270.8	2.22×10^{-12}

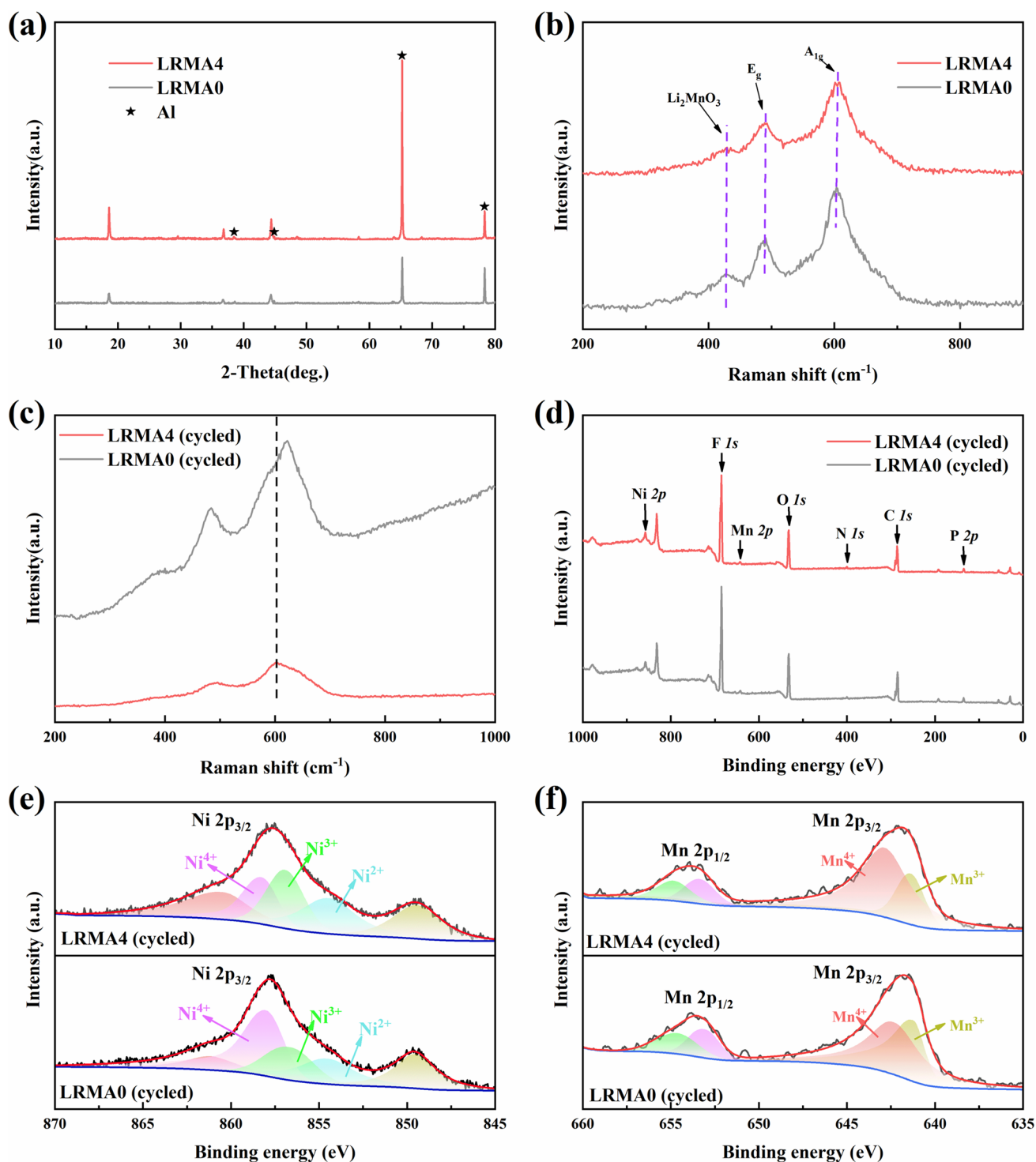


Fig. 9 **a** The ex situ X-ray diffraction patterns of LRMA0 and LRMA4 samples after 200 cycles. Raman spectra of **b** before cycling and **c** after 200 cycles for LRMA0 and LRMA4 samples. XPS spectra

of **d** survey scan, **e** Ni 2p and **f** Mn 2p for LRMA0 and LRMA4 samples after 200 cycles

element N came from NMP. In Fig. 9e, Ni 2p_{3/2} fit three peaks at approximately 854.8 eV, 856.6 eV, and 858.3 eV, which corresponded to Ni²⁺, Ni³⁺, and Ni⁴⁺, respectively

[59]. For comparison, the peak area of Ni⁴⁺ in the LRMA0 sample was the largest, which indicates that LRMA0 had more Ni⁴⁺. Ni⁴⁺ can cause oxidation reactions of materials,

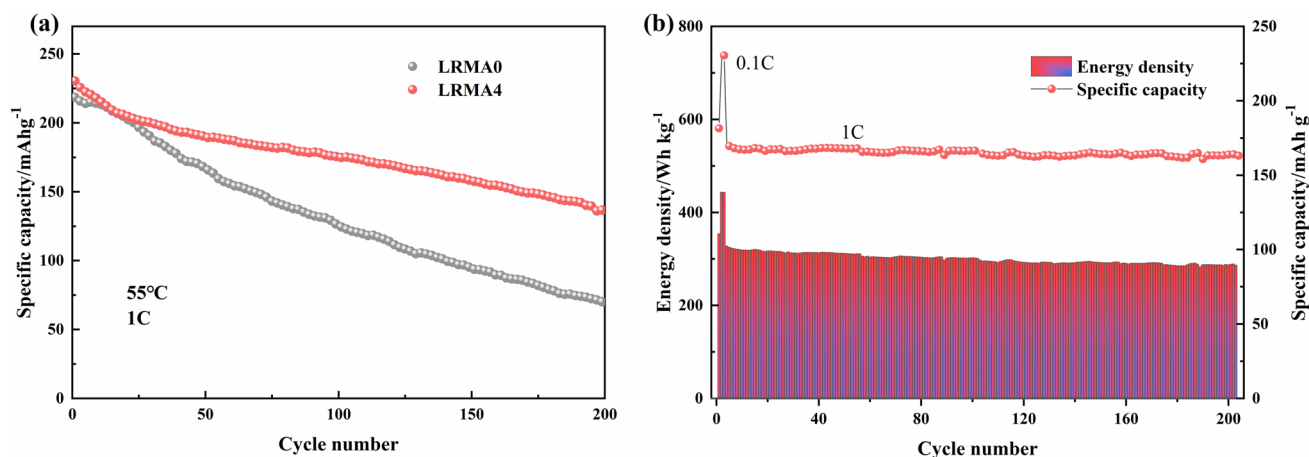


Fig. 10 **a** Cycling performance of LRMA0 and LRMA4 samples at 1 C and 55 °C. **b** Energy density and specific capacity of the LRMA4/graphite lithium-ion full cell. The specific energy density was calculated based on the mass of both active materials (cathode and anode)

which results in electrolyte decomposition and consumption of cathode active materials to decrease the performance [60] [47]. Fig. 9f displays the Mn 2p spectra of the LRMA0 and LRMA4 samples, and Mn $2p_{3/2}$ was fitted to the two peaks of Mn⁴⁺ and Mn³⁺. The fitting results show that LRMA0 contained more Mn³⁺. Mn³⁺ underwent a disproportionation reaction and induced the Jahn–Teller effect, which resulted in the loss of cathode active materials and structural collapse. Additionally, most significantly, the increase in Mn³⁺ decreased the DMV [47]; therefore, the LRMA4 sample showed less attenuation of DMV than LRMA0 in Fig. 6d. The reason is that the Al–O bond (512 kJ·mol⁻¹), which is stronger than the Mn–O bond (402 kJ·mol⁻¹), reduces oxygen release to reduce the production of Mn³⁺.

Finally, the high-temperature and full-cell performance of the samples were investigated, which are vital tests for any electrode material before commercialization. The cycling property of LRMA0 and LRMA4 samples at 1 C at 55 °C is described in Fig. 10a. The specific capacities of the LRMA0 and LRMA4 samples after 200 cycles were approximately 218.5 mAh·g⁻¹ and 230.4 mAh·g⁻¹, and the capacity retention rates were 31.9% and 59.1%, respectively. The cycle performance at high temperature improved because Al doping stabilized the sample structure. The electrochemical performance of the LRMA4 sample in lithium-ion full cells is shown in Fig. 10b. Commercial graphite was selected as the anode material, and the activation process was identical to that in Fig. 6c. Then, the full cell was performed at 1 C for the next 200 cycles. The specific capacity at 1 C was 170.53 mAh·g⁻¹, and the capacity retention rate was 95.6% after 200 cycles at 1 C, which is higher than that of the half cell (89.5%) due to the reduced electrode cross-talk [26]. The specific energy density, which was calculated based on potential profiles, displayed maximum values of approximately 443.7 Wh·kg⁻¹ at 0.1 C and approximately 328.1

Wh·kg⁻¹ at 1 C. After 200 cycles, the specific energy density was 286.9 Wh·kg⁻¹, and the retention rate was 87.4%. It is quite promising that the energy density of 200 Wh·kg⁻¹ could be maintained after 200 cycles at 1 C in commercial batteries, which is considered to satisfy the benchmark requirements of application in electric vehicles.

Conclusion

A series of Li_{1.2}Ni_{0.2}Mn_{0.6-x}Al_xO₂ (x = 0, 0.02, 0.04, 0.06) materials was synthesized using a modified Pechini method, and the results prove the effectiveness and feasibility of the Al doping strategy. The results show that doping Al reduces the transition from the layered structure to the spinel structure by lowering the unit cell parameters, reduces oxygen release by introducing stronger Al–O bonds, and suppresses the generation of Mn³⁺ during the cycle. The capacity retention rates of the LRMA2, LRMA4, and LRMA6 samples were 76.2%, 89.5%, and 81.1%, respectively, after 200 cycles at 1 C, while the capacity retention rate of LRMA0 was only 63.2%. Al doping can significantly inhibit the decay of the DMV during cycling, and the voltage decay of the LRMA4 sample was only 1.11 mV per cycle. The specific capacity of the Al-doped LRMA4 sample at 5 C reached 151 mAh·g⁻¹. Finally, the modified Pechini method can form a Li₂CO₃ coating on the surface of the material in situ using a one-step method, which decreases the cost. Thus, LRMA4 has the characteristics of fast charge–discharge performance, good cycle stability, and low cost, and it is an ideal choice for the next-generation lithium-ion battery.

Funding This work was financially supported by the Qian Ke He Ji Chu-ZK [2021]Yi Ban 236, the Guizhou Science and Technology

Planning Project [2020]5021, the Potential Subject Project of Guizhou University GZUQLXK21006, the Guizhou High Level and Innovative Talents Projects [2022]009–1, and the Natural Science Research Project of Guizhou Provincial Department of Education [2022]041.

Declarations

Conflict of interest The authors declare no competing interests.

References

- Hafiz H, Suzuki K, Barbiellini B, Tsuji N, Yabuuchi N, Yamamoto K, Orihara Y, Uchimoto Y, Sakurai Y, Sakurai H, Bansil A, Viswanathan V (2021) Tomographic reconstruction of oxygen orbitals in lithium-rich battery materials. *Nature* 594:213–216
- Sripad S, Viswanathan V (2017) Performance metrics required of next-generation batteries to make a practical electric semi truck. *ACS Energy Lett* 2:1669–1673
- Ye H, Li Y (2022) Towards practical lean-electrolyte Li–S batteries: highly solvating electrolytes or sparingly solvating electrolytes? *Nano Research Energy* 1:e9120012
- Liu Y, Li J, Shen Q, Zhang J, He P, Qu X, Liu Y (2022) Advanced characterizations and measurements for sodium-ion batteries with NASICON-type cathode materials. *eScience* 2(1):10–31
- Jia H, Li X, Song J, Zhang X, Luo L, He Y, Li B, Cai Y, Hu S, Xiao X, Wang C, Rosso KM, Yi R, Patel R, Zhang J-G (2020) Hierarchical porous silicon structures with extraordinary mechanical strength as high-performance lithium-ion battery anodes. *Nat Commun* 11:1174
- Chen D, Zhang W, Luo K, Song Y, Zhong Y, Liu Y, Wang G, Zhong B, Wu Z, Guo X (2021) Hard carbon for sodium storage: mechanism and optimization strategies toward commercialization. *Energy Environ Sci* 14:2244–2262
- Wang H, Wang C, Tang Y (2021) Interface engineering toward high-efficiency alloy anode for next-generation energy storage device. *EcoMat* 3:e12172
- Yang Z, Chen T, Chen D, Shi X, Yang S, Zhong Y, Liu Y, Wang G, Zhong B, Song Y, Wu Z, Guo X (2021) A Ge/carbon atomic-scale hybrid anode material: a micro-nano gradient porous structure with high cycling stability. *Angew Chem Int Ed Engl* 60:12539–12546
- Yang J, Li P, Zhong F, Feng X, Chen W, Ai X, Yang H, Xia D, Cao Y (2020) Suppressing voltage fading of Li-rich oxide cathode via building a well-protected and partially-protonated surface by polyacrylic acid binder for cycle-stable Li-ion batteries. *Adv Energy Mater* 10:1904264
- Ding X, Luo D, Cui J, Xie H, Ren Q, Lin Z (2020) An ultra-long-life lithium-rich $\text{Li}_{1.2}\text{Mn}_{0.6}\text{Ni}_{0.2}\text{O}_2$ cathode by three-in-one surface modification for lithium-ion batteries. *Angew Chem Int Ed Engl* 59:7778–7782
- Ye Z, Zhang B, Chen T, Wu Z, Wang D, Xiang W, Sun Y, Liu Y, Liu Y, Zhang J, Song Y, Guo X (2021) A simple gas-solid treatment for surface modification of Li-rich oxides cathodes. *Angew Chem Int Ed Engl* 60:23248–23255
- Tang Q, Dai X, Wang Z, Wu F, Mai Y, Gu Y, Deng Y (2021) Enhanced high-voltage performance of LiCoO_2 cathode by directly coating of the electrode with Li_2CO_3 via a wet chemical method. *Ceram Int* 47:19374–19383
- Chen Z-L, Gu Y-J, Luo G-Y, Huo Y-L, Wu F-Z (2022) Enhanced electrochemical performance of LiFePO_4/C wrapped with sulfur-modified reduced graphene oxide for Li-ion batteries. *Ionics* 28:191–200
- Luo G-Y, Gu Y-J, Liu Y, Chen Z-L, Huo Y-L, Wu F-Z, Mai Y, Dai X-Y, Deng Y (2021) Electrochemical performance of in situ LiFePO_4 modified by N-doped graphene for Li-ion batteries. *Ceram Int* 47:11332–11339
- Qiu B, Zhang M, Wu L, Wang J, Xia Y, Qian D, Liu H, Hy S, Chen Y, An K, Zhu Y, Liu Z, Meng YS (2016) Gas–solid interfacial modification of oxygen activity in layered oxide cathodes for lithium-ion batteries. *Nat Commun* 7:12108
- Cheng XB, Liu H, Yuan H, Peng HJ, Tang C, Huang JQ, Zhang Q (2021) A perspective on sustainable energy materials for lithium batteries. *SusMat* 1:38–50
- Lei Y, Ni J, Hu Z, Wang Z, Gui F, Li B, Ming P, Zhang C, Elias Y, Aurbach D, Xiao Q (2020) Surface modification of Li-rich Mn-based layered oxide cathodes: challenges, materials, methods, and characterization. *Adv Energy Mater* 10:2002506
- He W, Guo W, Wu H, Lin L, Liu Q, Han X, Xie Q, Liu P, Zheng H, Wang L, Yu X, Peng DL (2021) Challenges and recent advances in high capacity Li-rich cathode materials for high energy density lithium-ion batteries. *Adv Mater* 33:2005937
- Dong S, Zhou Y, Hai C, Zeng J, Sun Y, Ma Y, Shen Y, Li X, Ren X, Sun C, Zhang G, Wu Z (2020) Enhanced Cathode Performance: Mixed Al_2O_3 and LiAlO_2 Coating of $\text{Li}_{1.2}\text{Ni}_{0.13}\text{Co}_{0.13}\text{Mn}_{0.54}\text{O}_2$. *ACS Appl Mater Interfaces* 12:38153–38162
- Zheng J, Gu M, Xiao J, Polzin BJ, Yan P, Chen X, Wang C, Zhang J-G (2014) Functioning mechanism of AlF_3 coating on the Li- and Mn-rich cathode materials. *Chem Mater* 26:6320–6327
- Yang S-q, Wang P-b, Wei H-x, Tang L-b, Zhang X-h, He Z-j, Li Y-j, Tong H, Zheng J-c (2019) $\text{Li}_4\text{V}_2\text{Mn}(\text{PO}_4)_4$ -stabilized $\text{Li}_{1.2}\text{Mn}_{0.54}\text{Ni}_{0.13}\text{Co}_{0.13}\text{O}_2$ cathode materials for lithium ion batteries. *Nano Energy* 63:103889.
- Zhang W, Liu Y, Wu J, Shao H, Yang Y (2019) Surface modification of $\text{Li}_{1.2}\text{Mn}_{0.54}\text{Ni}_{0.13}\text{Co}_{0.13}\text{O}_2$ cathode material with $\text{Al}_2\text{O}_3/\text{SiO}_2$ composite for lithium-ion batteries. *J Electrochem Soc* 166:A863–A872
- Zhang P, Zhai X, Huang H, Zhou J, Li X, He Y, Guo Z (2020) Suppression of structural phase transformation of Li-rich Mn-based layered cathode materials with Na ion substitution strategy. *Electrochim Acta* 349:136402
- Xu H, Deng S, Chen G (2014) Improved electrochemical performance of $\text{Li}_{1.2}\text{Mn}_{0.54}\text{Ni}_{0.13}\text{Co}_{0.13}\text{O}_2$ by Mg doping for lithium ion battery cathode material. *J Mater Chem A* 2:15015–15021
- Chen J, Wang Y, Zhao N, Liu Z-Q (2019) Hierarchical micro-nanostructured and Al^{3+} -doped $\text{Li}_{1.2}\text{Ni}_{0.2}\text{Mn}_{0.6}\text{O}_2$ active materials with enhanced electrochemical properties as cathode materials for Li-ion batteries. *Scripta Mater* 171:47–51
- Wu F, Kim GT, Kuenzel M, Zhang H, Asenbauer J, Geiger D, Kaiser U, Passerini S (2019) Elucidating the effect of iron doping on the electrochemical performance of cobalt-free lithium-rich layered cathode materials. *Adv Energy Mater* 9:1902445
- Li L, Song BH, Chang YL, Xia H, Yang JR, Lee KS, Lu L (2015) Retarded phase transition by fluorine doping in Li-rich layered $\text{Li}_{1.2}\text{Mn}_{0.54}\text{Ni}_{0.13}\text{Co}_{0.13}\text{O}_2$ cathode material. *J Power Sources* 283:162–170
- Xie D, Li G, Li Q, Fu C, Fan J, Li L (2016) Improved cycling stability of cobalt-free Li-rich oxides with a stable interface by dual doping. *Electrochim Acta* 196:505–516
- Qiu L, Zhang M, Song Y, Xiao Y, Wu Z, Xiang W, Liu Y, Wang G, Sun Y, Zhang J, Zhang B, Guo X (2021) Recent advance in structure regulation of high-capacity Ni-rich layered oxide cathodes. *EcoMat* 3:e12141
- Nayak PK, Grinblat J, Levi M, Levi E, Kim S, Choi JW, Aurbach D (2016) Al Doping for mitigating the capacity fading and voltage decay of layered Li and Mn-rich cathodes for Li-ion batteries. *Adv Energy Mater* 6:1502398
- Yan W, Xie Y, Jiang J, Sun D, Ma X, Lan Z, Jin Y (2018) Enhanced rate performance of Al-doped Li-rich layered cathode

- material via nucleation and post-solvothermal method. *ACS Sustain Chem Eng* 6:4625–4632
32. Nayak PK, Penki TR, Markovsky B, Aurbach D (2017) Electrochemical performance of Li- and Mn-rich cathodes in full cells with prelithiated graphite negative electrodes. *ACS Energy Lett* 2:544–548
 33. Zhang C, Feng Y, Wei B, Liang C, Zhou L, Ivey DG, Wang P, Wei W (2020) Heteroepitaxial oxygen-buffering interface enables a highly stable cobalt-free Li-rich layered oxide cathode. *Nano Energy* 75:104995
 34. Zhang M, Qiu L, Sun Y, Song Y, Wu Z, Liu Y, Yang Z, Liu Y, Zhang J, Zhong B, Guo X (2021) Microstructure-controlled Li-rich Mn-based cathodes by a gas-solid interface reaction for tackling the continuous activation of Li_2MnO_3 . *ACS Appl Mater Interfaces* 13:40995–41003
 35. Wang D, Wu Z, Xiang W, Liu Y, Wang G, Hu K, Xu Q, Song Y, Guo X (2022) Is it universal that the layered-spinel structure can improve electrochemical performance? *J Energy Chem* 64:344–353
 36. Wang T, Zhang C, Li S, Shen X, Zhou L, Huang Q, Liang C, Wang Z, Wang X, Wei W (2021) Regulating anion redox and cation migration to enhance the structural stability of Li-rich layered oxides. *ACS Appl Mater Interfaces* 13:12159–12168
 37. Li M, Wang H, Zhao L, Zhou Y, Zhang F, He D (2019) Improving the electrochemical performance of lithium-rich oxide layer material with Mg and La co-doping. *J Alloys Compd* 782:451–460
 38. Zheng J, Ye Y, Liu T, Xiao Y, Wang C, Wang F, Pan F (2019) Ni/Li disordering in layered transition metal oxide: electrochemical impact, origin, and control. *Acc Chem Res* 52:2201–2209
 39. Li H, Jian Z, Yang P, Li J, Xing Y, Zhang S (2020) Niobium doping of $\text{Li}_{1.2}\text{Mn}_{0.54}\text{Ni}_{0.13}\text{Co}_{0.13}\text{O}_2$ cathode materials with enhanced structural stability and electrochemical performance. *Ceram Int* 46:23773–23779
 40. Yi T-F, Mei J, Peng P-P, Luo S (2019) Facile synthesis of polypyrrole-modified $\text{Li}_5\text{Cr}_7\text{Ti}_6\text{O}_{25}$ with improved rate performance as negative electrode material for Li-ion batteries. *Compos B Eng* 167:566–572
 41. Yi T-F, Qiu L-Y, Mei J, Qi S-Y, Cui P, Luo S, Zhu Y-R, Xie Y, He Y-B (2020) Porous spherical $\text{NiO}@\text{NiMoO}_4@\text{PPy}$ nanoarchitectures as advanced electrochemical pseudocapacitor materials. *Science Bulletin* 65:546–556
 42. Yang P, Li H, Wei X, Zhang S, Xing Y (2018) Structure tuned $\text{Li}_{1.2}\text{Mn}_{0.6}\text{Ni}_{0.2}\text{O}_2$ with low cation mixing and Ni segregation as high performance cathode materials for Li-ion batteries. *Electrochim Acta* 271:276–283
 43. Wei T-T, Peng P, Ji Y-R, Zhu Y-R, Yi T-F, Xie Y (2022) Rational construction and decoration of $\text{Li}_5\text{Cr}_7\text{Ti}_6\text{O}_{25}@\text{C}$ nanofibers as stable lithium storage materials. *J Energy Chem* 71:400–410
 44. Tf Yi, Shi L, Han X, Wang F, Zhu Y, Xie Y (2020) Approaching high-performance lithium storage materials by constructing hierarchical $\text{CoNiO}_2\text{CeO}_2$ nanosheets. *Energy Environ Mater* 4:586–595
 45. Yin C, Zhou H, Yang Z, Li J (2018) Synthesis and electrochemical properties of $\text{LiNi}_{0.5}\text{Mn}_{1.5}\text{O}_4$ for Li-ion batteries by the metal-organic framework method. *ACS Appl Mater Interfaces* 10:13625–13634
 46. Fu X, Xia Z, Zhao D, Liang Y, Wang P, Zhang N, Tuo K, Lu H, Cai X, Mao L, Li S (2021) Study on electrochemical performance of Al-substitution for different cations in Li-rich Mn-based materials. *Electrochim Acta* 394:139136
 47. Hu E, Yu X, Lin R, Bi X, Lu J, Bak S, Nam K-W, Xin HL, Jaye C, Fischer DA, Amine K, Yang X-Q (2018) Evolution of redox couples in Li- and Mn-rich cathode materials and mitigation of voltage fade by reducing oxygen release. *Nat Energy* 3:690–698
 48. Csernica PM, Kalirai SS, Gent WE, Lim K, Yu Y-S, Liu Y, Ahn S-J, Kaeli E, Xu X, Stone KH, Marshall AF, Sinclair R, Shapiro DA, Toney MF, Chueh WC (2021) Persistent and partially mobile oxygen vacancies in Li-rich layered oxides. *Nat Energy* 6:642–652
 49. Zhang P, Zhai X, Huang H, Zhou J, Li X, He Y, Guo Z (2020) Synergistic Na^+ and F^- co-doping modification strategy to improve the electrochemical performance of Li-rich $\text{Li}_{1.20}\text{Mn}_{0.54}\text{Ni}_{0.13}\text{Co}_{0.13}\text{O}_2$ cathode. *Ceram Int* 46:24723–24736
 50. Chen G, An J, Meng Y, Yuan C, Matthews B, Dou F, Shi L, Zhou Y, Song P, Wu G, Zhang D (2019) Cation and anion Co-doping synergy to improve structural stability of Li- and Mn-rich layered cathode materials for lithium-ion batteries. *Nano Energy* 57:157–165
 51. Xu Y, Zhang M, Yi L, Liang K (2021) Fe^{3+} and PO_4^{3-} co-doped Li-rich $\text{Li}_{1.20}\text{Mn}_{0.56}\text{Ni}_{0.16}\text{Co}_{0.08}\text{O}_2$ as cathode with outstanding structural stability for lithium-ion battery. *J Alloys Compd* 865:158899
 52. Ma Q, Chen Z, Zhong S, Meng J, Lai F, Li Z, Cheng C, Zhang L, Liu T (2021) Na-substitution induced oxygen vacancy achieving high transition metal capacity in commercial Li-rich cathode. *Nano Energy* 81:105622
 53. Jiang W, Zhang C, Feng Y, Wei B, Chen L, Zhang R, Ivey DG, Wang P, Wei W (2020) Achieving high structure and voltage stability in cobalt-free Li-rich layered oxide cathodes via selective dual-cation doping. *Energy Storage Mater* 32:37–45
 54. Tang W, Duan J, Xie J, Qian Y, Li J, Zhang Y (2021) Dual-site doping strategy for enhancing the structural stability of lithium-rich layered oxides. *ACS Appl Mater Interfaces* 13:16407–16417
 55. Sallard S, Billaud J, Sheptyakov D, Novak P, Villevieille C (2020) Cr-doped Li-rich nickel cobalt manganese oxide as a positive electrode material in Li-ion batteries to enhance cycling stability. *ACS Appl Energy Mater* 3:8646–8657
 56. Xu Z, Ci L, Yuan Y, Nie X, Li J, Cheng J, Sun Q, Zhang Y, Han G, Min G, Lu J (2020) Potassium Prussian blue-coated Li-rich cathode with enhanced lithium ion storage property. *Nano Energy* 75:104942
 57. Nayak PK, Grinblat J, Levi M, Haik O, Levi E, Aurbach D (2015) Effect of Fe in suppressing the discharge voltage decay of high capacity Li-rich cathodes for Li-ion batteries. *J Solid State Electr* 19:2781–2792
 58. Liu S, Liu Z, Shen X, Li W, Gao Y, Banis MN, Li M, Chen K, Zhu L, Yu R, Wang Z, Sun X, Lu G, Kong Q, Bai X, Chen L (2018) Surface doping to enhance structural integrity and performance of Li-rich layered oxide. *Adv Energy Mater* 8:1802105
 59. Shi J-L, Zhang J-N, He M, Zhang X-D, Yin Y-X, Li H, Guo Y-G, Gu L, Wan L-J (2016) Mitigating voltage decay of Li-rich cathode material via increasing Ni content for lithium-ion batteries. *ACS Appl Mater Interfaces* 8:20138–20146
 60. Sim S-J, Lee S-H, Jin B-S, Kim H-S (2021) Effects of lithium tungsten oxide coating on $\text{LiNi}_{0.90}\text{Co}_{0.05}\text{Mn}_{0.05}\text{O}_2$ cathode material for lithium-ion batteries. *J Power Sources* 481:229037

Publisher's Note Springer Nature remains neutral with regard to jurisdictional claims in published maps and institutional affiliations.

Springer Nature or its licensor (e.g. a society or other partner) holds exclusive rights to this article under a publishing agreement with the author(s) or other rightsholder(s); author self-archiving of the accepted manuscript version of this article is solely governed by the terms of such publishing agreement and applicable law.